Supporting Information

Simultaneous sulfite electrolysis and hydrogen production using Ni foam-based three-dimensional electrodes

Raúl A. Márquez-Montes[†], *Kenta Kawashima*[††], *Kobe M. Vo*[‡], *David Chávez-Flores*[†], *Virginia H. Collins-Martínez*[‡‡], *C. Buddie Mullins*[††,‡,§], and *Víctor H. Ramos-Sánchez*[†,‖,*]

[†] Facultad de Ciencias Químicas, Universidad Autónoma de Chihuahua, Chihuahua, Chihuahua 31125, México.

[††] Department of Chemistry, The University of Texas at Austin, Austin, Texas 78712, United States.

[‡] McKetta Department of Chemical Engineering, The University of Texas at Austin, Austin, Texas 78712, United States.

[‡‡] Centro de Investigación en Materiales Avanzados, Chihuahua, Chihuahua 31136, México

[§] McKetta Department of Chemical Engineering, Texas Materials Institute, and Center for Electrochemistry, The University of Texas at Austin, Austin, Texas 78712, United States.

[‖] Department of Mechanical and Aerospace Engineering, University of California San Diego, La Jolla, California 92093, United States.

* Corresponding author: vramos@uach.mx; vramossanchez@ucsd.edu

Number of pages: 38

Number of figures: 22

Number of tables: 2

Detailed Experimental Methods

Materials

Ni foam (99.99%, 80 - 110 ppi) with a thickness of 1.6 mm was purchased from MTI Co. Pd/C (10 wt% Pd loading), Pt gauze (99.9%, 52 mesh) and palladium chloride ($PdCl_2$) were purchased from Merck KGaA Co. FAA-3 hydroxyl anion exchange ionomer (10 wt% in N-methyl-2-pyrrolidone) and FAA-3-50 anion exchange membrane (AEM) with a thickness of 50 μm were purchased from FuMATech GmbH. Ammonium chloride (NH_4Cl), ammonium hydroxide (NH_4OH), ammonium sulfite monohydrate ($(NH_4)_2SO_3 \cdot H_2O$), ammonium sulfate ($(NH_4)_2SO_4$), potassium peroxydisulfate ($K_2S_2O_8$) and potassium hydroxide (KOH) were purchased from Alfa Aesar. All the aqueous solutions were prepared with deionized water (DIW).

Cleaning of NF substrates

NF pieces (50 × 30 × 1.6 mm) were cleaned sequentially in 50 mL of the following solutions while in an ultrasonic bath for 15 min each: (1) acetone, (2) ethanol, (3) 3 M HCl and (4) DIW.

Preparation of NiO/Ni/NF electrodes

Clean NF pieces were immersed in 0.15 M $K_2S_2O_8$ solution for 8 hours. For each synthesis, two 50 × 30 × 1.6 mm pieces were immersed in 50 mL of solution. After 8 hours, the solution exhibited a greenish color, which was attributed to the partial dissolution of Ni due to a chemical etching process done by the oxidizing agent: $K_2S_2O_8$. The NF exhibited almost the same color, and extensive oxidation of the NF was not observed (see electrodes photos, Figure S1).

Preparation of Pd/NF electrodes

To achieve a homogeneous and reproducible electrodeposition of Pd over the NF, the latter was loaded into our previously reported electrochemical flow cell in a membrane-less configuration. A detailed description of the cell is given elsewhere.[1] Pt gauze (one mesh, 50 × 30 mm) and NF were used as the anode and cathode, respectively. A constant separation of 4 mm was achieved by stacking square-shaped turbulence promoters. The palladium plating solution (2.7 mM $PdCl_2$, 0.35 M NH_4Cl) was recirculated at 8 $L \cdot h^{-1}$. Concentrated NH_4OH solution (28% w/w) was added until the pH was 8.5. Then, a constant current density of 10 $mA \cdot cm^{-2}$ was applied for 30 minutes. The NF was removed, rinsed with DI water, dried for two hours at room temperature, and stored in a vacuum desiccator at 25°C. The Pd loading on NF was estimated by measuring Pd concentration in the spent plating bath using Total reflectance X-ray fluorescence (TXRF). Electrodes are shown in Figure S1.

Preparation of Pd/C/NF electrodes

Pd/C/NF electrodes were prepared by a spray-coating method using a mixture of Pd/C in a water/isopropanol/ionomer mixture, as detailed in a previous work.[2] The NF was coated with catalytic ink using an air-assisted spray gun. Four coating layers were applied for each side, with a drying period of two hours at room temperature between layer coating. Coatings were applied at 7 cm (between the spray gun and the NF) at an angle of 60° in a serpentine pattern (diameter of the spray dot: 8 - 10 mm). The NF was kept in position by using a homemade spraying set up, consisting of a perforated plastic plate connected to a vacuum hose, which provided a constant suction below the NF. A Pd loading of 0.54 ± 0.12 $mg \cdot cm^{-2}$ was estimated by checking the weight difference. Representative electrodes are shown in Figure S1.

Material characterization

Crystallographic structure of the as-prepared electrode materials was assessed by X-ray diffraction (XRD) using a Rigaku MiniFlex 600 X-ray diffractometer, in the range from 20 to 80 2θ degree. Scanning electron microscopy (SEM) was conducted to observe the resultant morphologies of the electrode surfaces and cross-sections in a FEI Quanta 650 microscope. The electrode cross-sections were prepared with a Hitachi IM4000Plus ion milling system. Energy-dispersive X-ray spectroscopy (EDX) was performed to obtain elemental mappings, and X-ray photoelectron spectroscopy (XPS) was used to investigate surface chemical composition employing a Kratos AXIS Ultra DLD spectrometer. The carbon 1s major peak of adventitious carbon at 285 eV was used to correct/verify the binding energies of the elements of interest. XPS data were processed by using CasaXPS software.

Preparation of small Ni foam electrodes for electrochemical characterization

Small NF pieces (10 × 20 × 1.6 mm) were used to prepare representative anodes for electrochemical characterization. These NF substrates were covered with a solid polydimethylsiloxane case to expose only 1 cm^2 and to avoid electrolyte penetration. The area to be covered was completely flattened and a Cu wire, as current collector, was fixed. Approximately 3 g of encapsulants in a 10:1 ratio (SYLGARD™ 184 Silicone Elastomer Kit, Dow Corning) was mixed thoroughly for 10 min and subsequently dried in a vacuum oven for 15 minutes at 50°C until it was viscous. The mixture was applied until it covered the Cu wire contact. Electrodes were left to dry for 24 hours at room temperature. Once the rest of the piece was encapsulated, electrodes were prepared by the same procedures: electrodeposition (Pd/NF), spray coating with Pd/C (Pd/C/NF), chemical oxidation (NiO/Ni/NF).

Electrochemically active surface area estimation using 1 cm^2 electrodes

The active surface area was estimated by checking the double-layer capacitance (C_{DL}) of small NF electrodes. The open circuit potential (OCP) was registered for 300 s. Afterwards, eight CV scans (at ±50 mV around the OCP) were recorded from 200 to 10 mV·s^{-1}. The current at each scan rate in the middle of the potential window was chosen as the non-faradaic capacitive current density. Cathodic and anodic currents were averaged and plotted against the scan rate, giving the linear behavior of an ideal capacitor. The slope of the fitted line was associated to the value of C_{DL}, which was compared between electrodes. Note: this procedure was performed using only the supporting electrolyte solution (see next section). Results are shown in Figure S9.

Characterization of the redox behavior using 1 cm^2 electrodes

Electrodes were tested in a 150 mL jacketed cell (Gamry) using a three-electrode configuration: NF electrode, graphite rod and Ag/AgCl electrodes as working, auxiliary and reference electrodes, respectively. Cyclic voltammetry (CV) scans were recorded between -0.8 and 1.25 V *vs.* Ag/AgCl at 10 mV·s^{-1}. Ohmic drop was measured by means of the current-interruption technique. Two electrolytes were used: 0.5 M ammonium sulfate supporting electrolyte and 50 mM ammonium sulfite + 0.5 M ammonium sulfate. Phosphate salts (Na_2HPO_4 and KH_2PO_4) were added to the electrolytes to achieve a 10 mM buffer (KPi). pH was carefully measured with a glass electrode, and it was stable around 8.51 ± 0.6 throughout the tests. Electrolytes were purged with Ar gas for 15 min prior testing. Results are shown in Figure S10.

Determination of sulfite concentration in the anolyte

Samples taken every two hours from the anolyte container were analyzed in a SO_3^{2-} sensor. A total of 10 μL of Fe-free 1.0 M KOH solution (pH ~14) were mixed with 40 μL of the sample and mixed. The mixture was placed on a DRP-110 screen-printed electrode (DropSens). Linear sweep voltammetry (LSV) scans from 0.10 to 0.75 V *vs.* Ag pseudo reference electrode were recorded. The current at 0.715 V of the 3rd scan was compared to an external calibration curve (Figure S5) to estimate the concentration of SO_3^{2-} ion. Note: a 5/4 dilution factor was considered.

Hydrogen production measurements

Hydrogen gas production was measured by gas chromatography with thermal conductivity detector (GC-TCD) as described previously.[3] A total of 200 μL from the headspace was sampled at regular intervals using gas-tight syringes (pressure-lok 1 mL RN) and injected into the gas chromatograph with a HaySep N 80/100; Carboxen 1000 60/80 column (PerkinElmer®). Hydrogen content was determined by comparing the area under the curve (AUC) of the hydrogen peak in each chromatogram (1.43 min) against a hydrogen volume fraction calibration curve.

Estimation of the C_{DL} during performance tests

Electrolysis was stopped every two hours, and the electrolyte was recirculated for 5 min to dissipate bubbles. Then, the open circuit potential (OCP) was registered for 5 min without recirculation to define the non-faradaic region. Afterwards, eight CV scans (±50 mV around the OCP) were recorded with different scan rates: 200 to 10 $mV \cdot s^{-1}$. Cathodic and anodic currents at the center potential were averaged and plotted against the scan rate, giving the linear behavior of an ideal capacitor. The slope of the fitted line was associated with the value of C_{DL}.

Calculation of faradaic efficiencies (FEs)

For sulfite electrooxidation, FEs were estimated as depicted in Equation S1:

$$\mathrm{FE} = \frac{(n_0 - n_t) \cdot z \cdot \mathrm{F} \cdot (1000)}{j \cdot \mathrm{A} \cdot t}(100) \quad \text{(S1)}$$

where n_0 represents the initial moles of SO_3^{2-}, n_t denotes the moles of SO_3^{2-} at time *t*, F is Faraday's constant (96485.3 C mol^{-1}), *z* is the number of electrons transferred (2 for SO_3^{2-}), *j* is the applied current density (10 mA cm^{-2}), *A* is the geometric electrode area (15 cm^2) and *t* the time in seconds.

For hydrogen production, FEs were estimated as follows:

$$\mathrm{FE} = \frac{n_{H2} \cdot z \cdot \mathrm{F} \cdot (1000)}{j \cdot \mathrm{A} \cdot t}(100) \quad \text{(S2)}$$

where n_{H2} is the number of moles of H_2 generated every two hours (according to GC-TCD). In this case, *z* equals 2 for H_2 production, and t was always equal to 7200 seconds.

Calculation of reaction rates

Reaction rates for sulfite electrooxidation and H_2 production were calculated according to the rate of change in the number of moles of a component, based on unit surface:[4]

$$\mathrm{r}_i = \frac{1}{\mathrm{S}}\frac{dn_i}{dt} = \frac{moles\ of\ i\ produced\ or\ consumed}{(surface)(time)} \quad \text{(S3)}$$

and based on unit volume of reacting fluid:

$$\mathrm{r}_i = \frac{1}{\mathrm{V}}\frac{dn_i}{dt} = \frac{moles\ of\ i\ produced\ or\ consumed}{(volume\ of\ fluid)(time)} \quad \text{(S4)}$$

For sulfite electrooxidation, the number of moles was determined from the sulfite concentration registered every 2 hours with the amperometric sensor and the calibration curve. The difference corresponds to the number of moles consumed during a period of 2 hours. Volume was assumed to be constant as 250 cm^3. Note that the volumetric reaction rate corresponds to the slope of every pair of points in the sulfite concentration curve with time (Figure 4e, bottom). Therefore, twelve reaction rates (*i.e.,* twelve slopes) were estimated and shown in Figure 4b. For H_2 production, moles in the headspace were quantified using GC-TCD every 2 hours of electrolysis. The number of H_2 moles produced in this period of time were substituted in Equations S3 and S4 to obtain reaction rates.

Calculation of performance metrics

The performance metrics shown in Table 1 in the main document are described as follows.[5] The space-time yield is a measure of the productivity (in moles or mass) by unit reactor volume in units of time, and it is estimated as follows:

$$\mathrm{Y}_{ST} = \frac{j \cdot \mathrm{A}}{z \cdot \mathrm{F} \cdot V_R}(\mathrm{FE}) \tag{S5}$$

where V_R is the total reactor volume (250 cm^3). Y_{ST} is measured in $mol \cdot cm^{-3} \cdot s^{-1}$. Note that if the geometric area and the reactor volume are removed in Equation S5, the productivity in terms of the geometric area is obtained.

The energy yield can be estimated by using Equation S4:

$$\mathrm{Y}_E = \frac{3.6 \times 10^6}{z \cdot \mathrm{F} \cdot V_C}(\mathrm{FE}) \tag{S6}$$

where V_C is the cell voltage (~2.0 V). Y_E is measured in mol·kW·h^{-1}. Finally, the energy consumption can be estimated as follows:

$$E_C = \frac{1}{Y_E} \quad \text{(S7)}$$

which is measured in kW·h·mol^{-1}.

Finally, electrolyzer efficiency was estimated by using Equation S8:[6]

$$\eta_{Elec} = \frac{n_{H2} \cdot HHV}{P_{in}}(100) \quad \text{(S8)}$$

where n_{H2} is the hydrogen production rate (mol·h^{-1}, considering an electrode area of 15 cm^2), HHV is the higher heating value of hydrogen (0.079 kW·h·mol^{-1}, which corresponds to a value of 285.8 kJ·mol^{-1}) and P_{in} is the applied power (in kW). For calculation, operation for one hour is considered. Also, pumping power is about 0.010 kW·h.

Supporting Tables and Figures

Figure S1. Digital photos of large electrodes (a) before and (b) after electrooxidation tests.

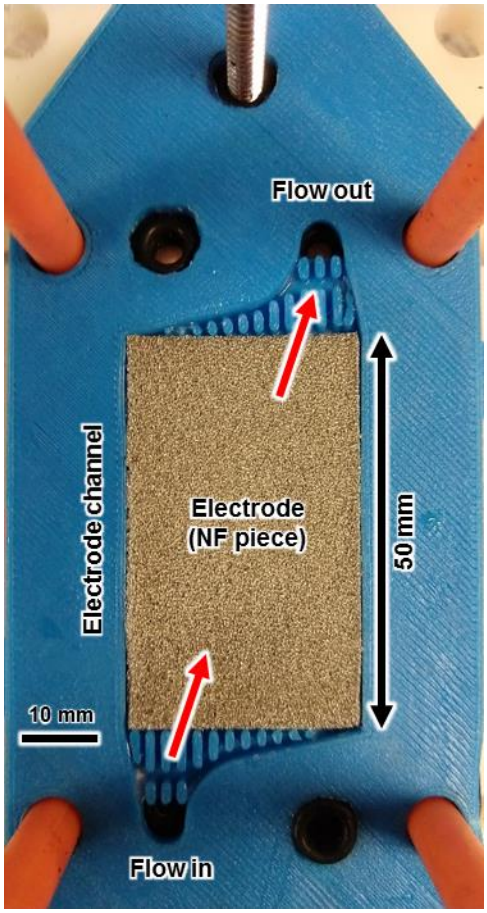

Figure S2. Digital photo depicting a NF piece installed as 3D electrode in the flow cell.

Table S1. Typical properties of effluents from the absorption step in the FGD process.

Gas phase temperature (K)	SO_2 inlet concentration ($mg \cdot m^{-3}$)	Liquid phase temperature (K)	pH	SO_3^{2-} concentration (mM)	Ref.
363	-	383	-	-	[7]
-	2857 – 11429	293	-	30 – 100	[8]
-	2857 – 11429	313	-	30 – 100	[8]
-	-	303 - 333	4.5 – 6.5	4 – 26	[9]
353	1767	-	-	-	[10]
293 - 353	5000	298	-	~ 58	[11]
-	-	323	5.0 – 6-0	1900 – 2300	[12]
298*	600 - 2400	298*	4.0 – 6.0	1560 – 1700*	[13]
-	-	323	5.9 – 11.0	25 - 45	[14]

Notes: *Assumed values from plots/further explanation required; these values correspond to specifications and properties of FGD studies in the literature. Values from commercial units may vary due to the application, type of fuel, flue gas composition, size of scrubbing units, or additional unit operations for further purification.

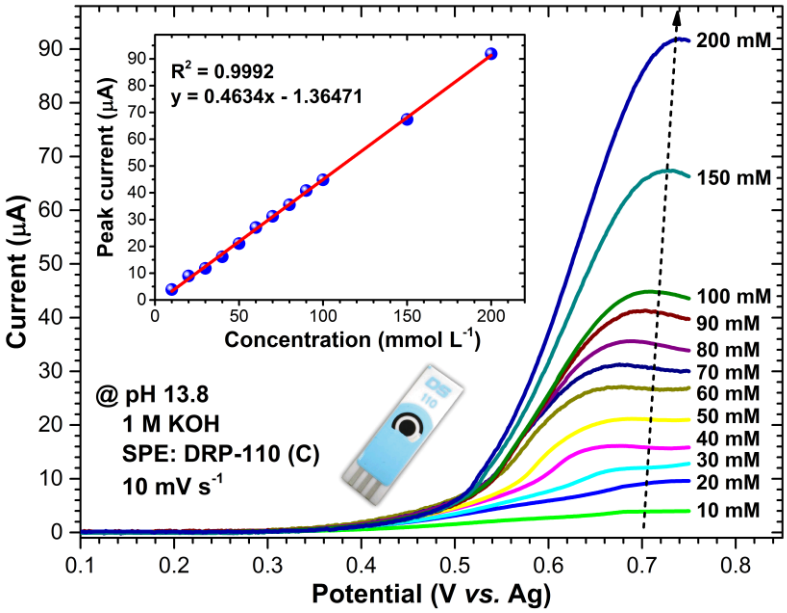

Figure S3. LSV calibration curve used during electrooxidation tests to quantify SO_3^{2-} concentration.

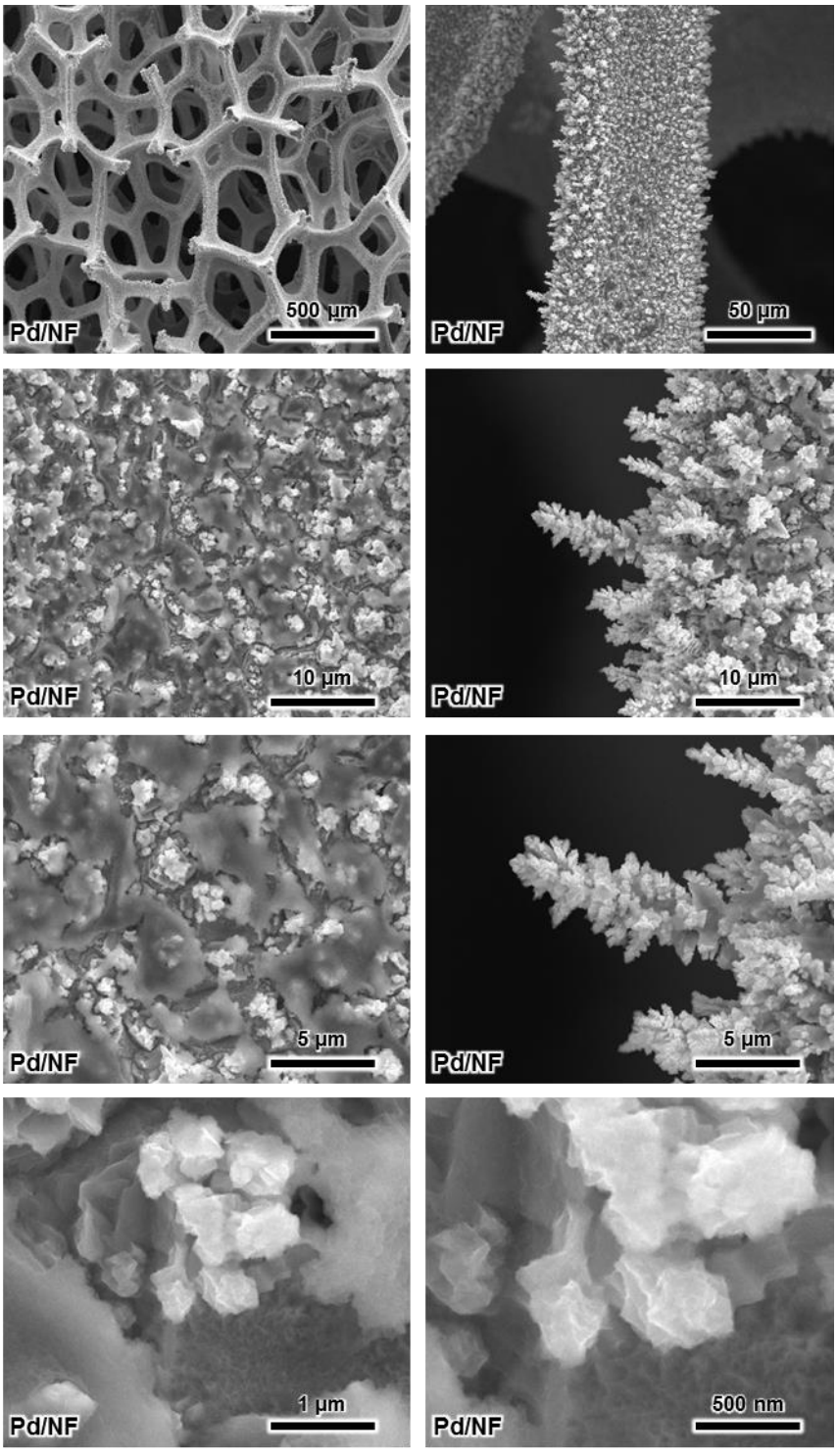

Figure S4. Full SEM characterization of Pd/NF electrode (anode) at different magnifications before electrolysis.

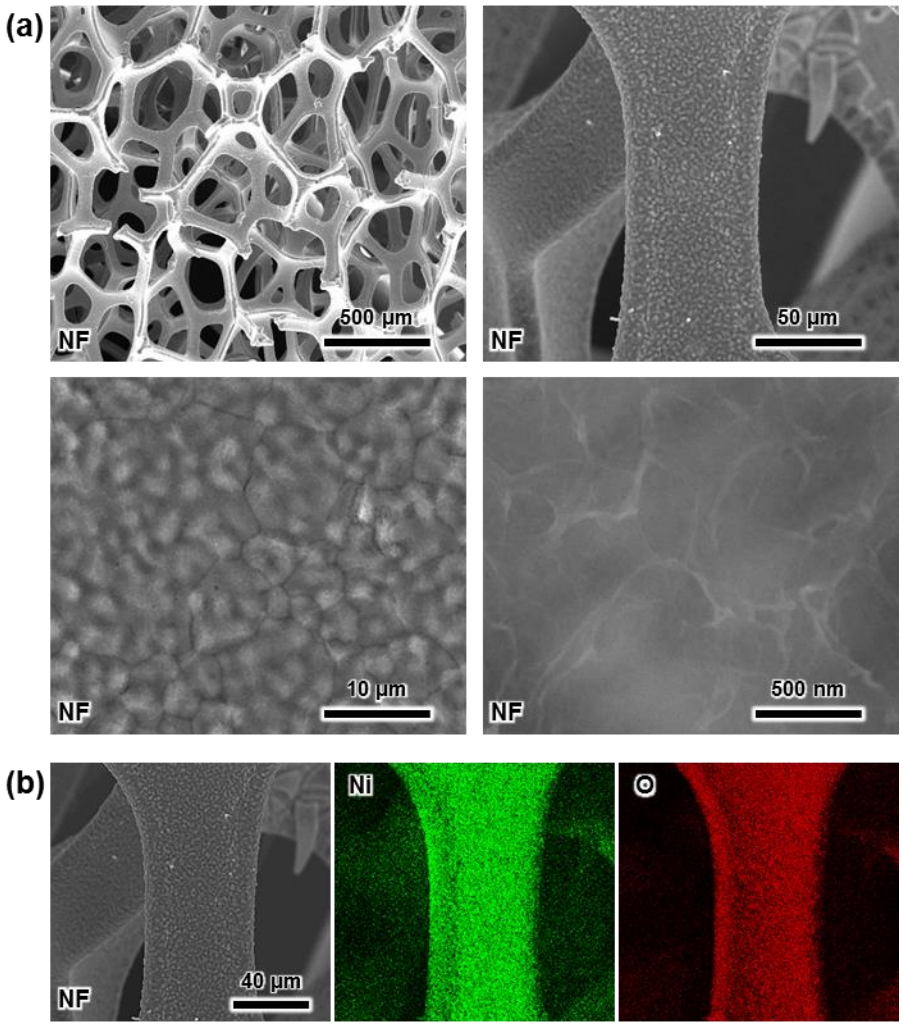

Figure S5. Characterization of pristine NF: (a) SEM images at different magnifications and (b) elemental mapping.

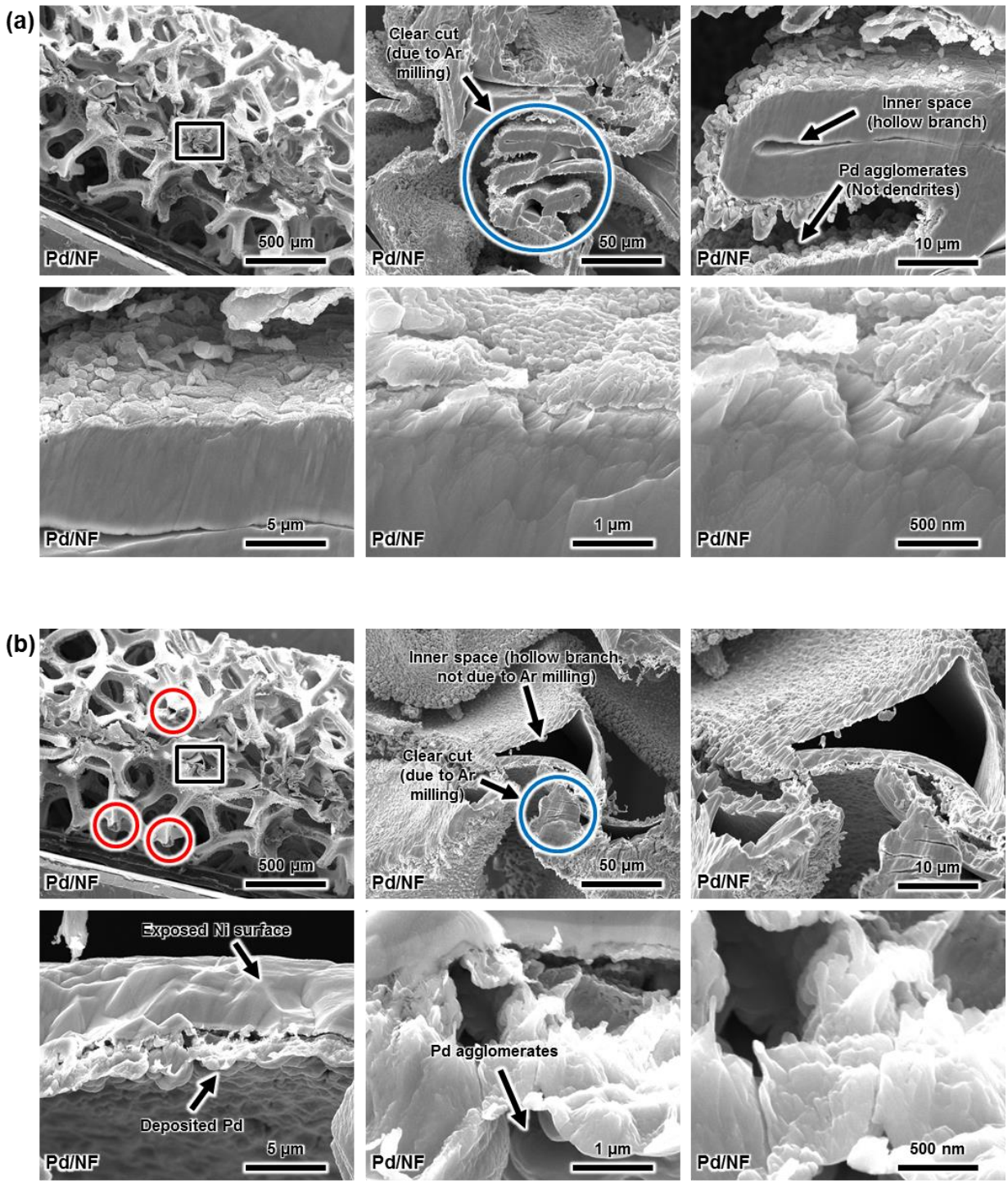

Figure S6. Additional SEM images of Pd/NF electrodes in different zones: (a) cross-sectional view of a clear-cut area due to Ar ion milling and (b) cross-sectional view of a hollow NF branch. Note: blue circles denote Ar ion milling cuts, while red circles denote already-exposed inner spaces within the NF. Black squares denote magnification areas.

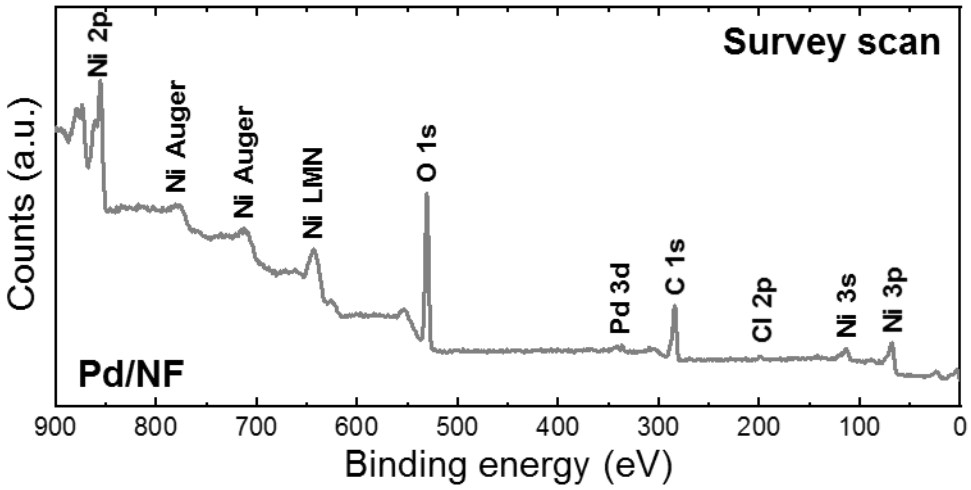

Figure S7. XPS analysis of the Pd/NF electrode. For the Pd/NF sample, only the survey scan was provided because high-valence Pd species can be reduced into Pd metal due to X-ray exposure.

In the Pd/NF electrode, Pd, Ni, O, and Cl peaks are confirmed.[15] This suggests that the Pd/NF surface consists primarily of Pd metal, oxidized Ni and Pd species, $PdCl_2$, and organic impurities which may arise from ethanol/acetone washing procedure after synthesis.

Table S2. Atomic composition (%) from EDX spectra on NF branches before (Figure 5d) and after (Figure 6b) electrolysis. Note: remaining percentages (not shown) are due to Al and C (sample holder).

Element	Before	After
Pd/NF (anode)		
Pd	32.13	79.58
Ni	10.07	10.40
O	43.53	6.07
NiO/Ni/NF (cathode)		
Ni	83.20	73.22
O	3.06	10.87
S	0.08	0.37
Pristine NF (blank)		
Ni	99.21	-
O	1.98	-

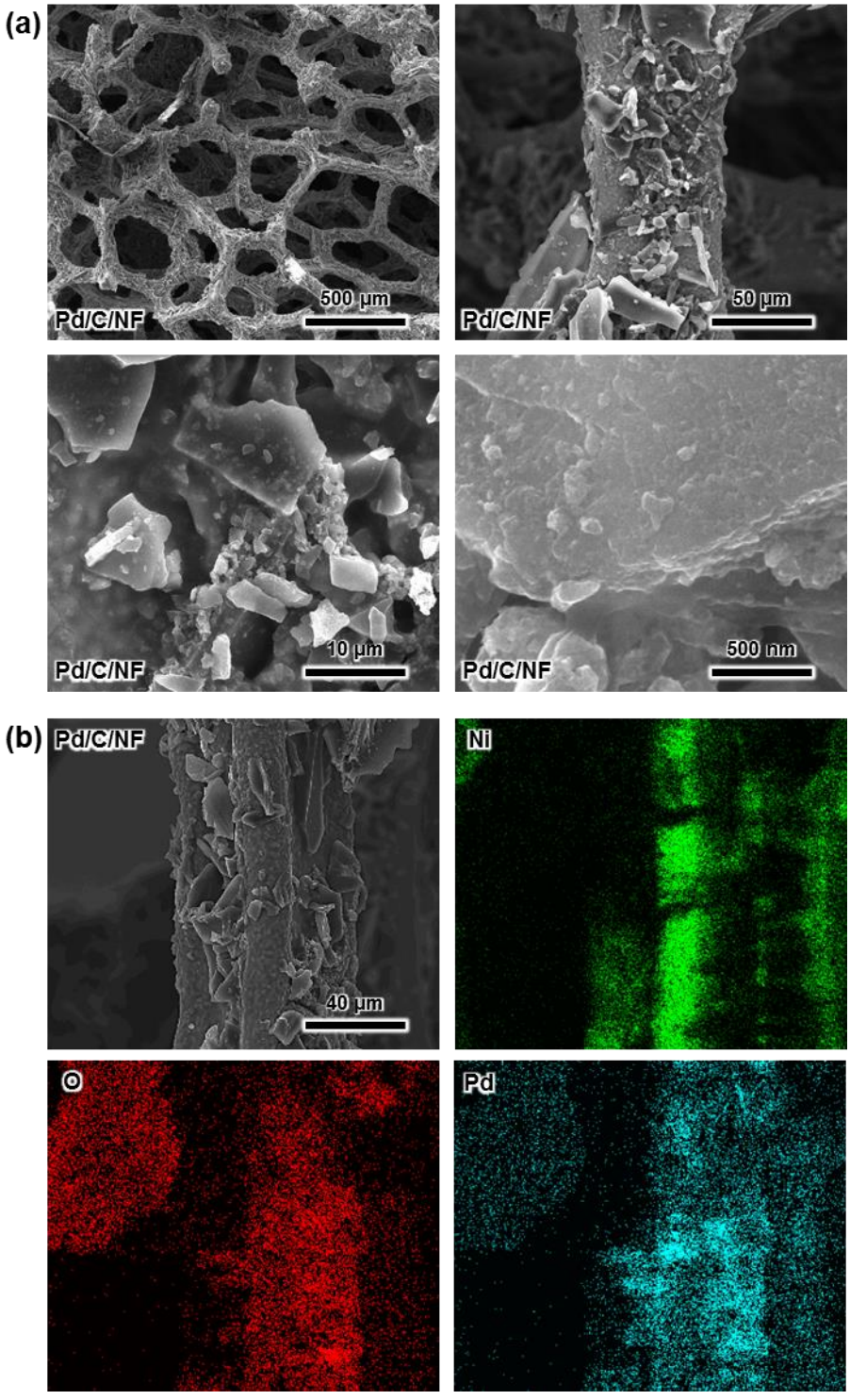

Figure S8. Characterization of Pd/C/NF electrode (anode): (a) SEM images at different magnifications and (b) elemental mapping.

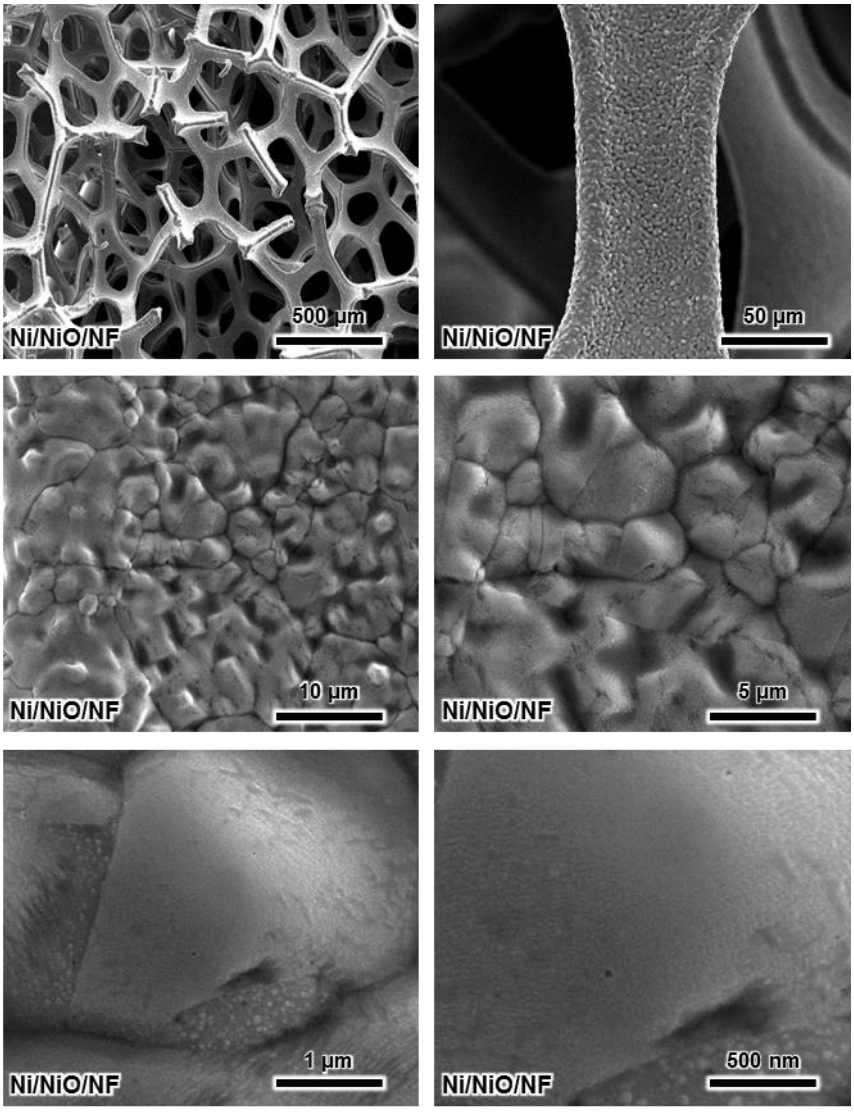

Figure S9. Full SEM characterization of NiO/Ni/NF electrode (cathode) at different magnifications before electrolysis.

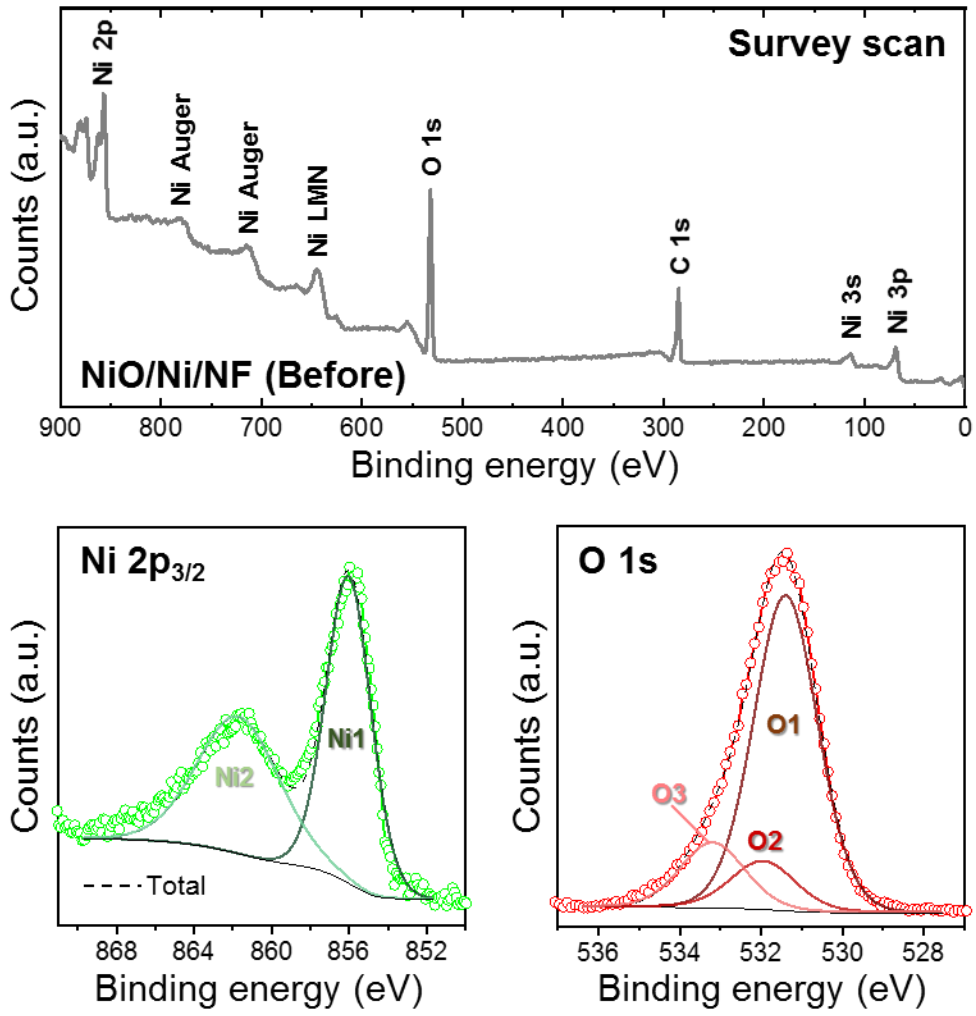

Figure S10. XPS analysis of the NiO/Ni/NF electrode before electrolysis.

Peak analysis is described as follows. The Ni $2p_{3/2}$ peaks can be attributed to Ni^{2+} in $Ni(OH)_2$ [at ~ 855 eV (Ni1)] and satellites [at ~ 861 eV (Ni2)],[16,17] In the O 1s spectrum of the fresh NiO/Ni/NF (Figure S10), the three components noted at ~ 531 (O1), ~ 532 (O2), and ~ 533 eV (O3) can be assigned to the O^{2-} anions in $Ni(OH)_2$, O=C linkage, and O–C linkage, respectively.[16–18] Overall, the surface of the fresh NiO/Ni/NF was mainly composed of $Ni(OH)_2$ and some organic impurities, also arising from ethanol/acetone washing.

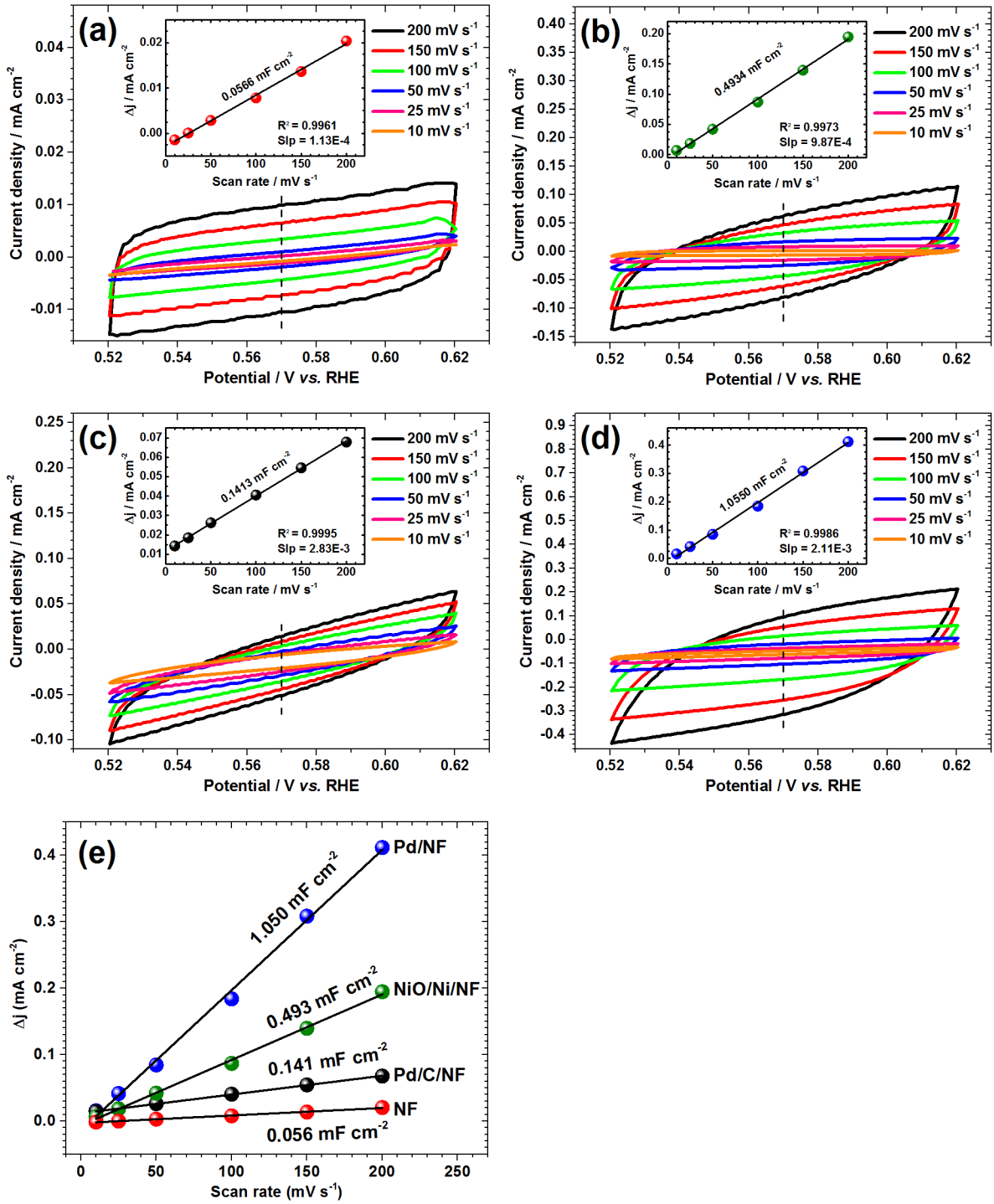

Figure S11. ECSA estimation of prepared electrodes: (a) bare NF, (b) NiO/Ni/NF, (c) Pd/C/NF, (d) Pd/NF and (e) comparison of C_{DL} values for each electrode (slopes).

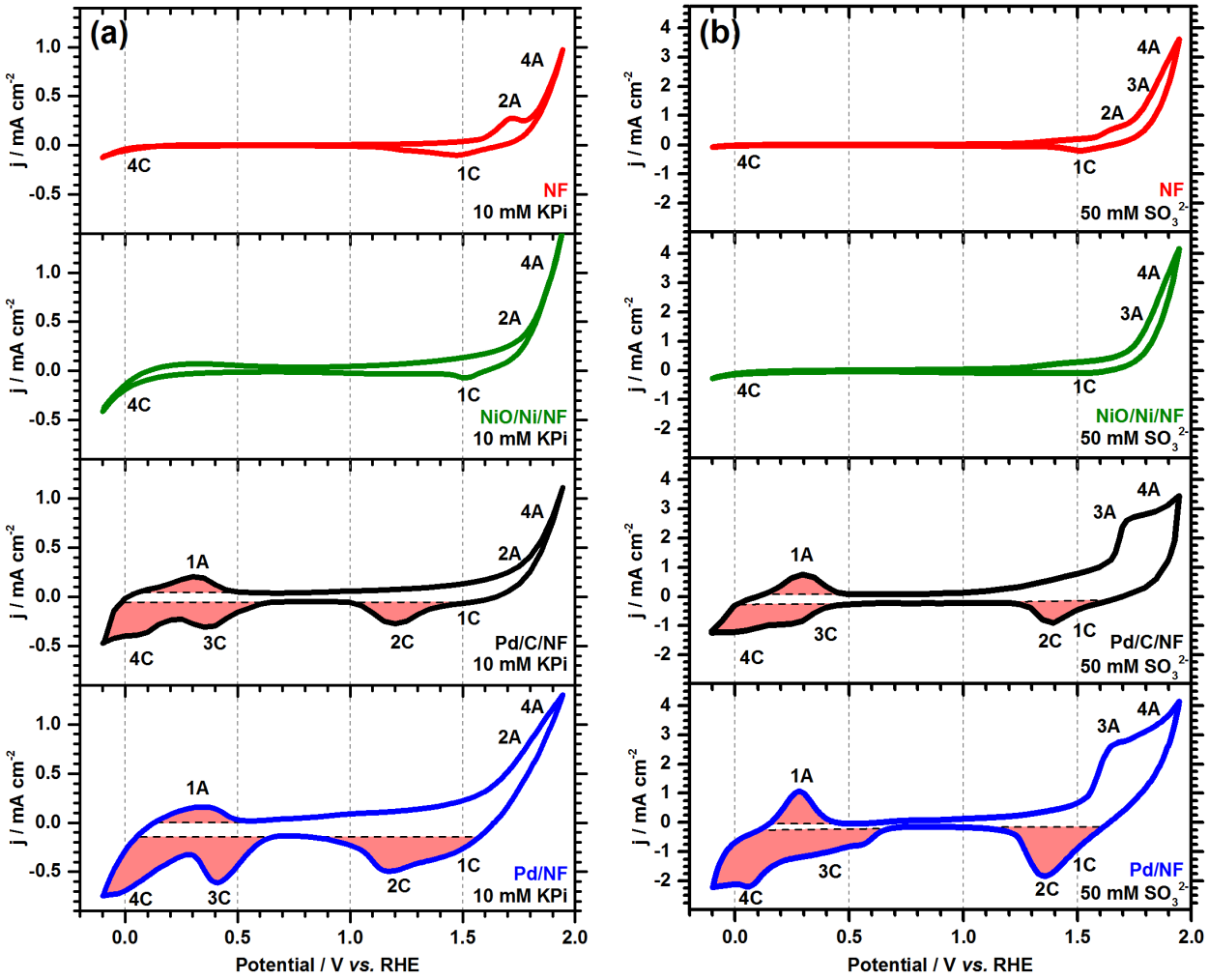

Figure S12. CV scans for definition of redox processes on prepared electrodes: (a) only supporting electrolyte and (b) 50 mM SO_3^{2-} with supporting electrolyte.

Only Pd/NF and Pd/C/NF electrodes exhibit noticeable signals for SO_3^{2-} electrooxidation (Peak 3A in the lower (b) panel).[2] Other peaks are related to Pd surface oxides reduction (Peak 2C in Fig. S10),[19,20] as well as hydrogen adsorption (Peak 3C) and desorption (Peak 1A) in the Pd lattice interstices.[21–23] Note that such peaks for the Pd/NF show larger colored areas than those for the Pd/C/NF, which denotes a substantial increase of the number of Pd active sites. This is attributed to the high-quality Pd microstructures achieved by the electrodeposition method. Besides the Pd/NF, some Pd active sites could be buried below stacked layers in the Pd/C/NF

prepared by spray coating. This is in good accord with the ECSA results, in which Pd/NF displayed the highest ECSA value. The oxygen evolution reaction (OER) and HER appear as peaks (Peak 4A 2C in Fig. S10) and (Peak 4C), respectively. In the case of the pristine NF and NiO/Ni/NF electrodes, transformation of β-$Ni(OH)_2$ into β-NiOOH (2A) and the reverse process (Peak 1C) are evident.[21,24] A higher activity towards the HER and OER is noticeable for the NiO/Ni/NF compared to the pristine NF, which reinforces the idea of use as a cathode in our system. Furthermore, Ni was not substantially active towards SO_3^{2-} oxidation, and no other redox process was observed in the evaluated electrodes. Accordingly, the Pd/NF was the best anode due to its superior ECSA and large number of Pd active sites.

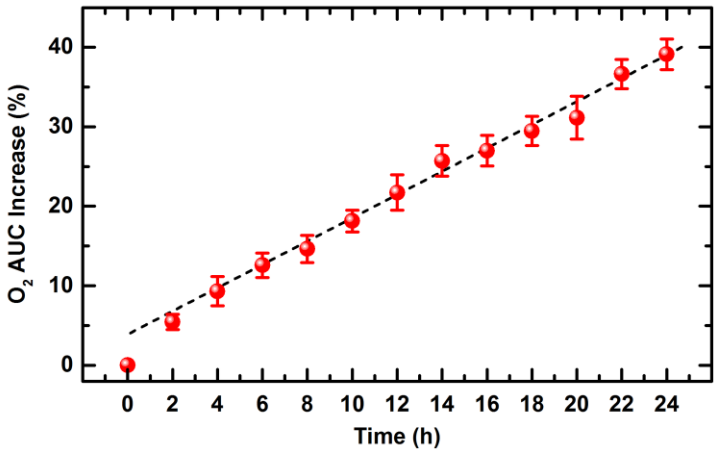

Figure S13. Percentage increase of oxygen signals from chromatograms (as AUC) in gas samples taken at the catholyte container's headspace and analyzed *via* GC-TCD.

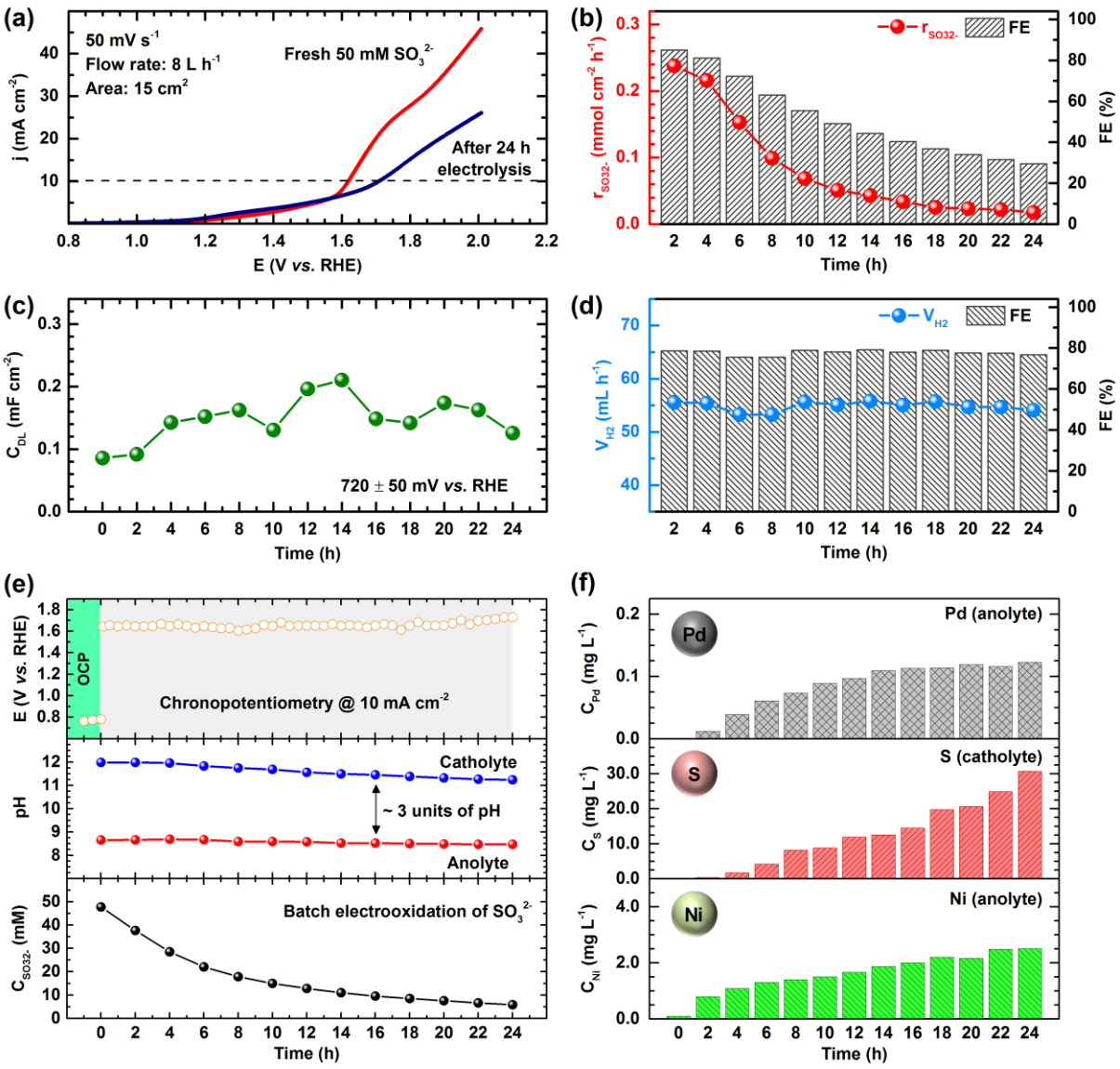

Figure S14. Electrooxidation test at 10 mA·cm^{-2} using Pd/C/NF electrodes.

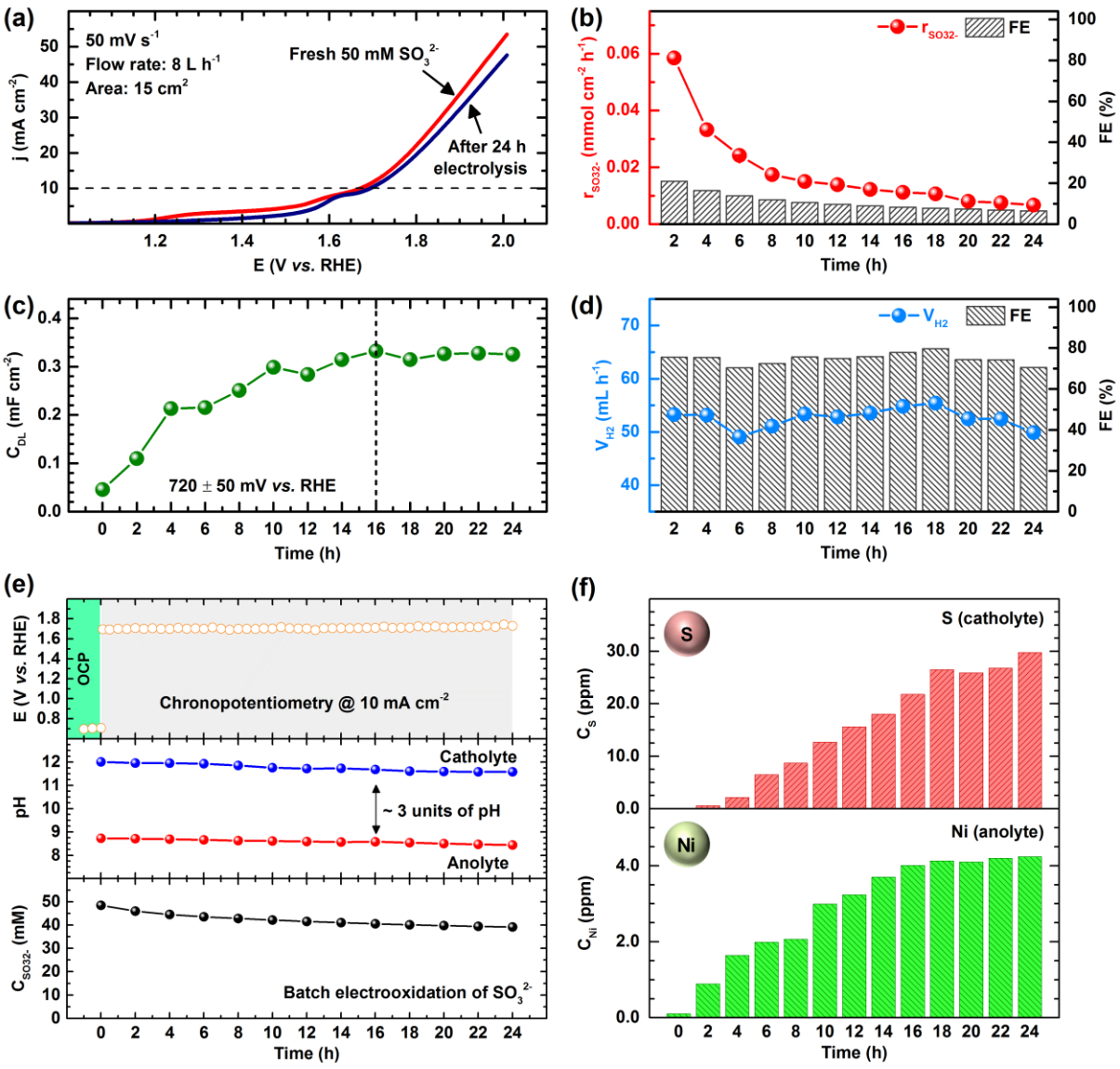

Figure S15. Electrooxidation test at 10 mA·cm^{-2} using bare NF electrodes.

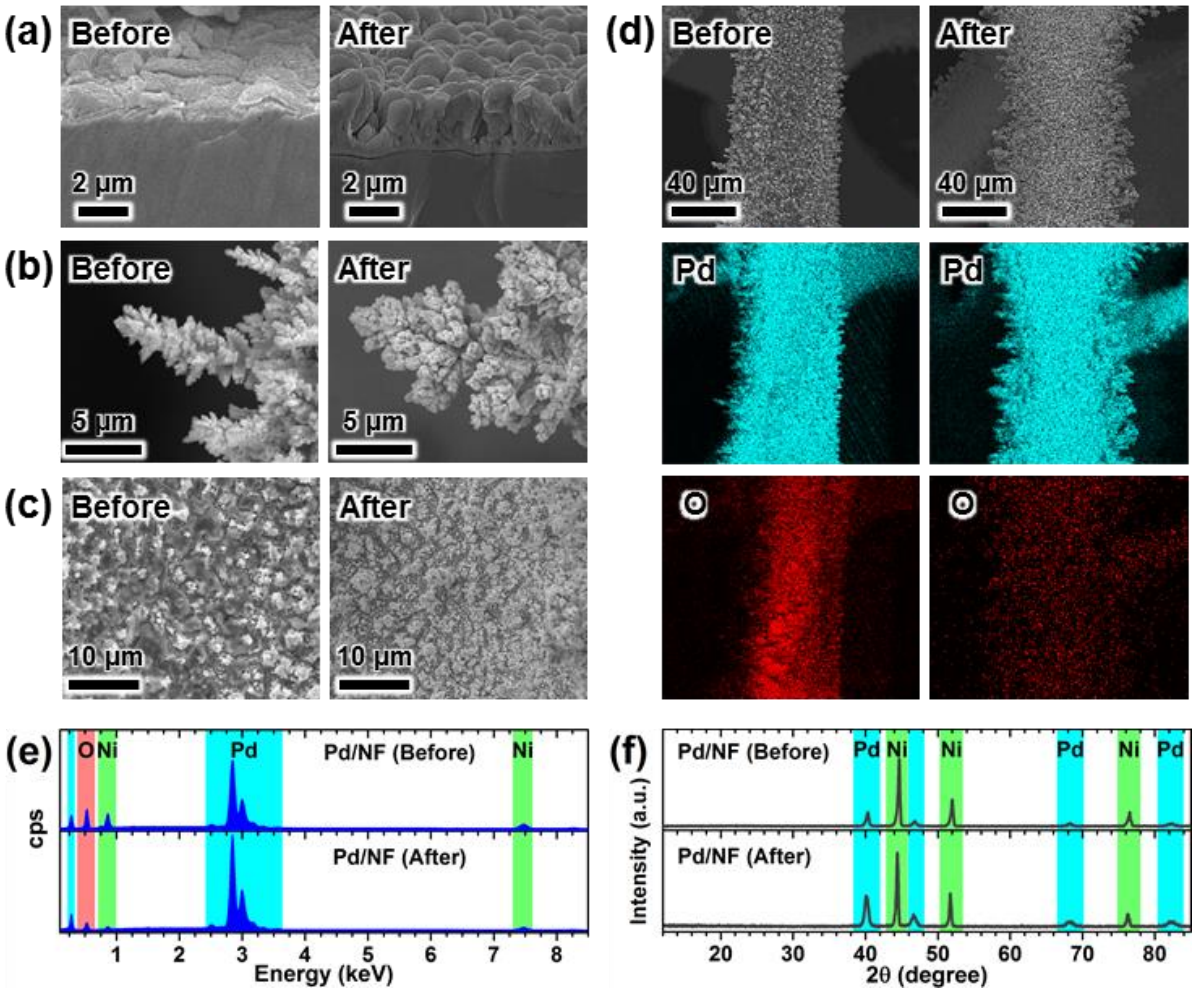

Figure S16. Stability results before and after electrolysis for Pd/NF electrode: SEM images for (a) cross section, (b) Pd dendrite, and (c) Pd/NF branch, (d) elemental mapping for Pd/NF branch, (e) EDX spectra at Pd/NF branch and (f) XRD results.

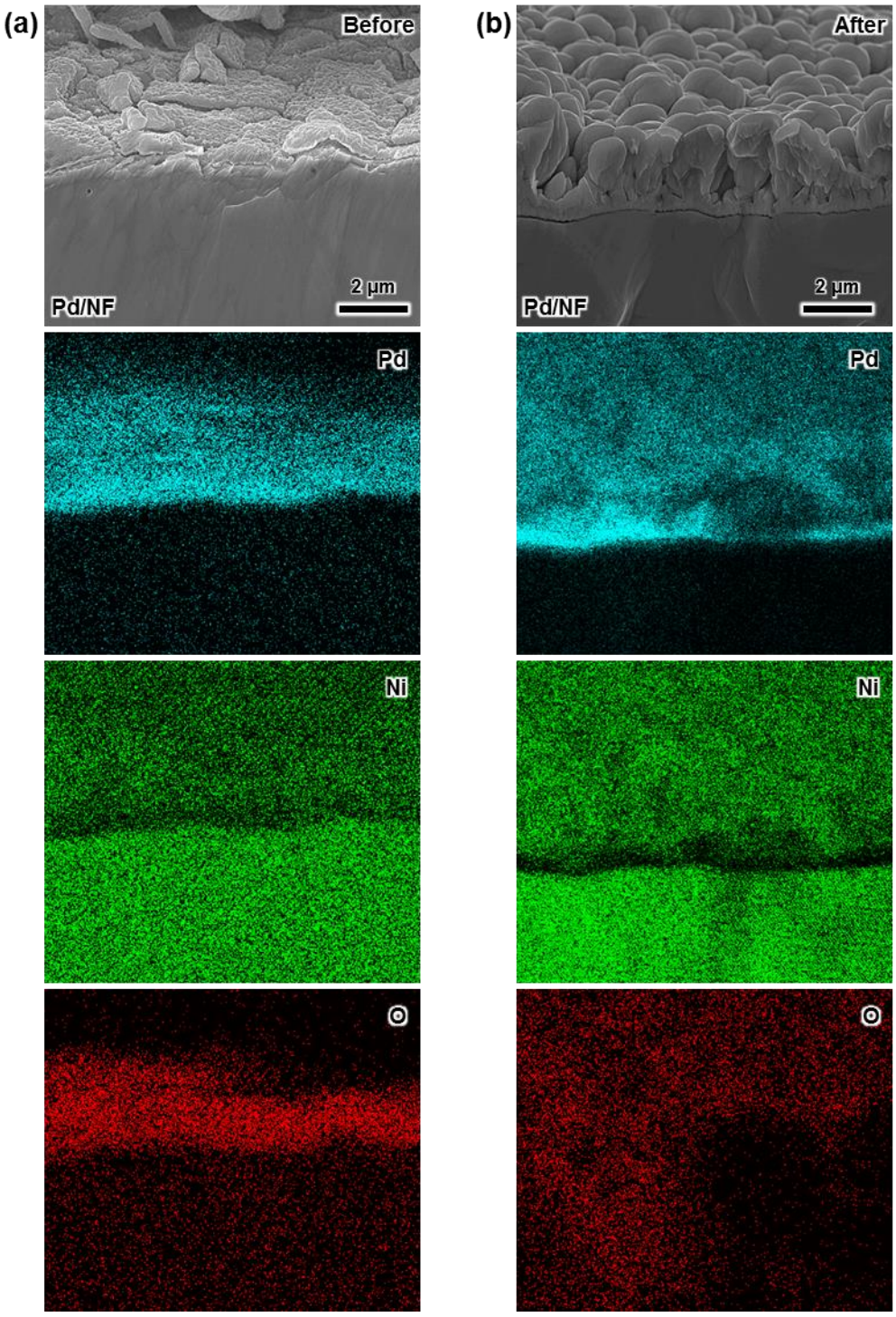

Figure S17. Elemental mapping of Pd/NF cross-sections (a) before and (b) after electrolysis.

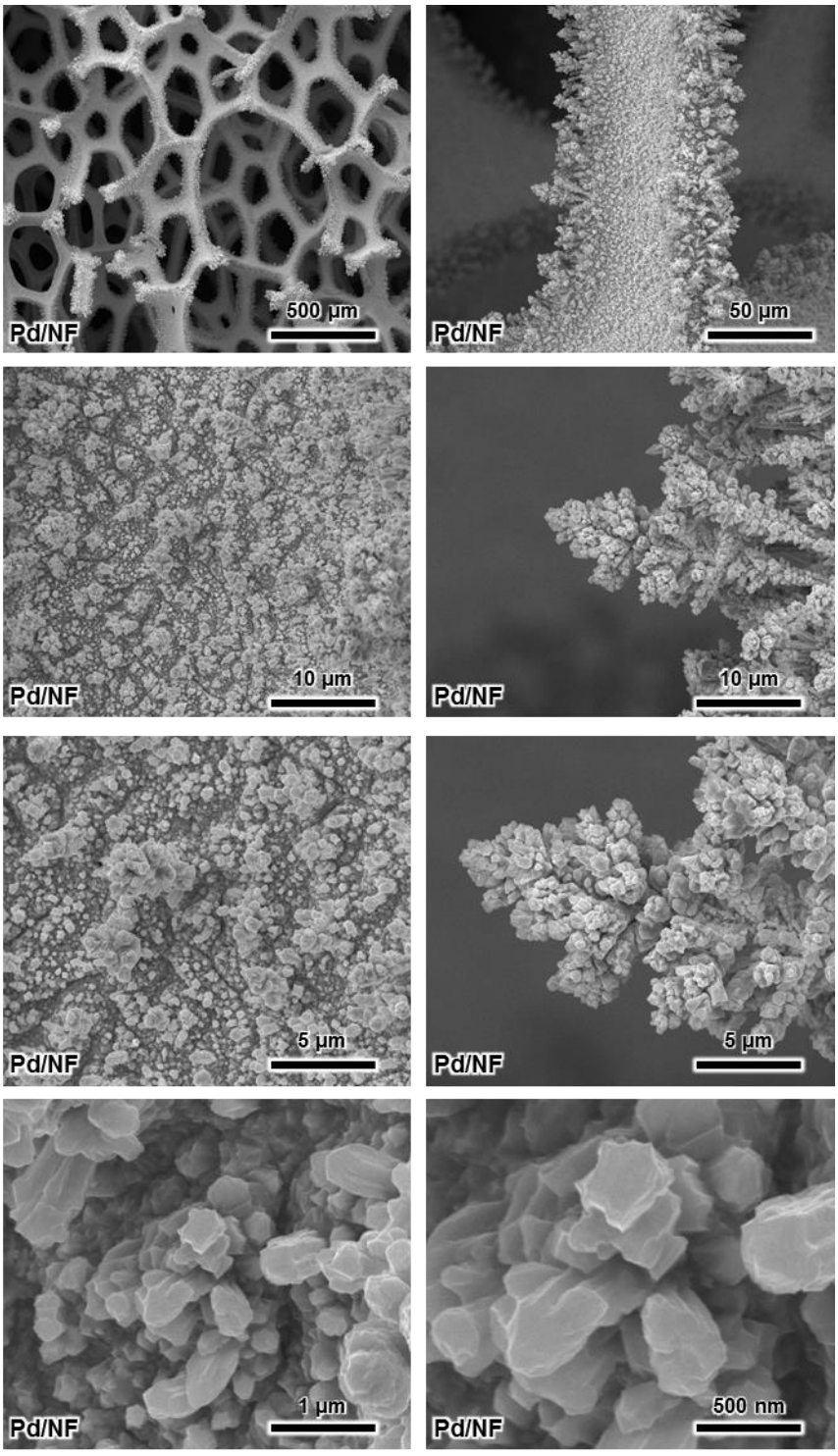

Figure S18. Full SEM characterization of Pd/NF electrode (anode) at different magnifications after electrolysis.

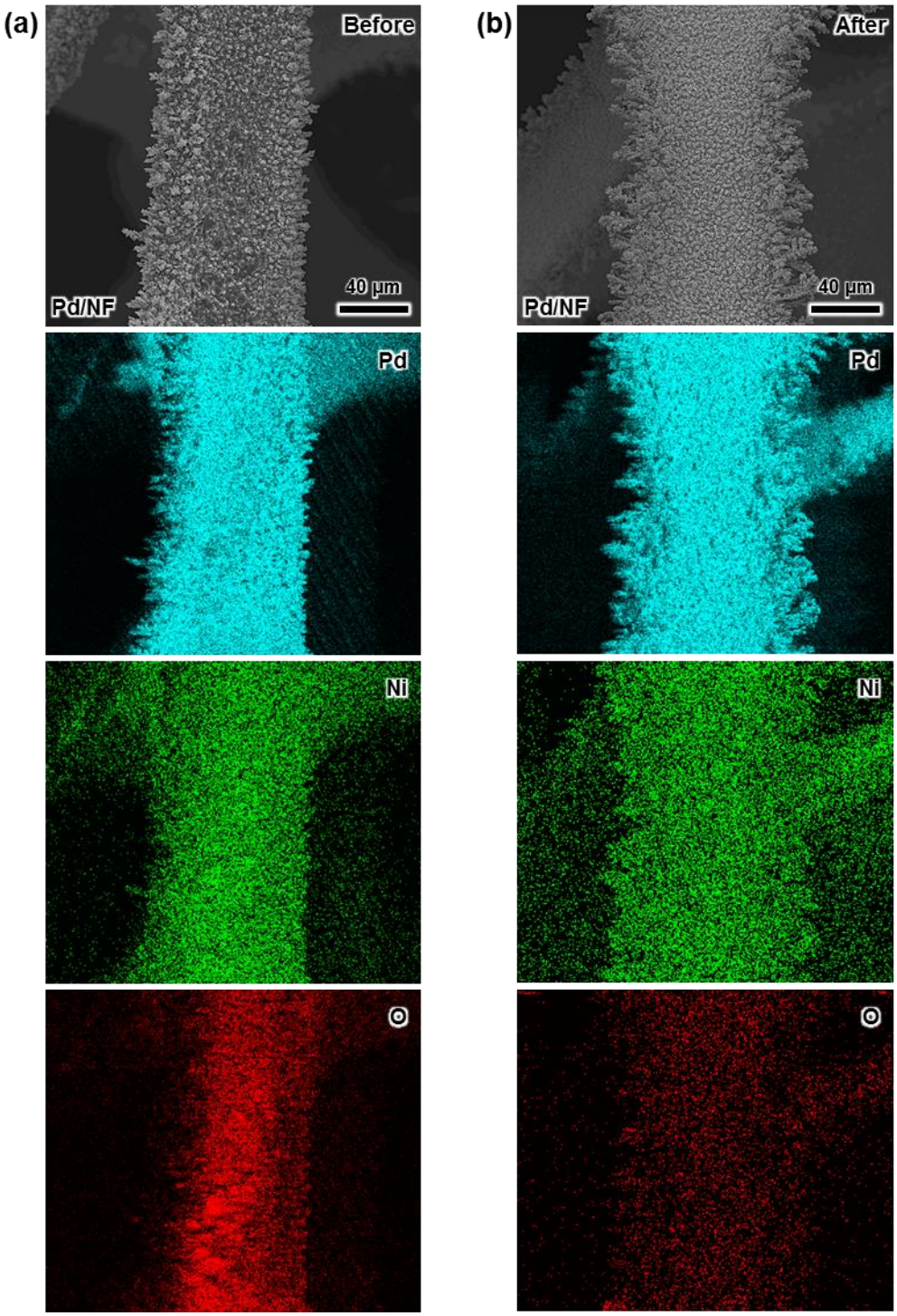

Figure S19. Elemental mapping of Pd/NF branch (a) before and (b) after electrolysis.

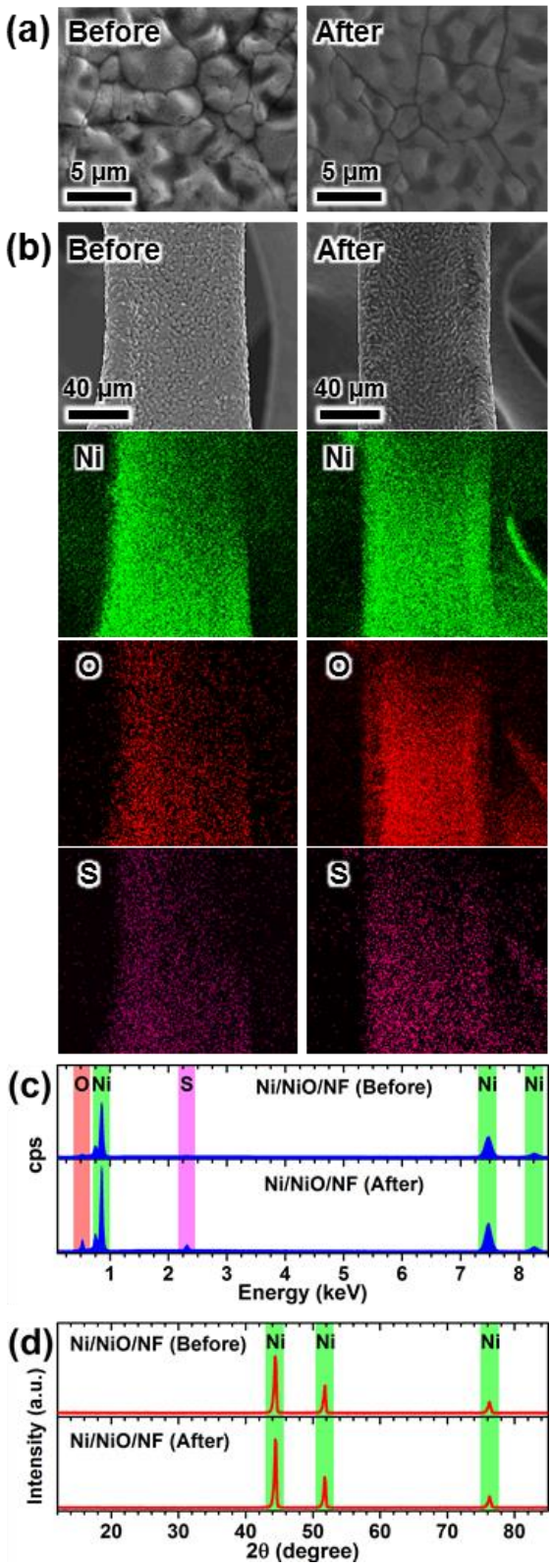

Figure S20. Stability results before and after electrolysis for NiO/Ni/NF electrode: (a) SEM images and (b) elemental mapping for NiO/Ni/NF branch, (c) EDX spectra at NiO/Ni/NF branch and (d) XRD results.

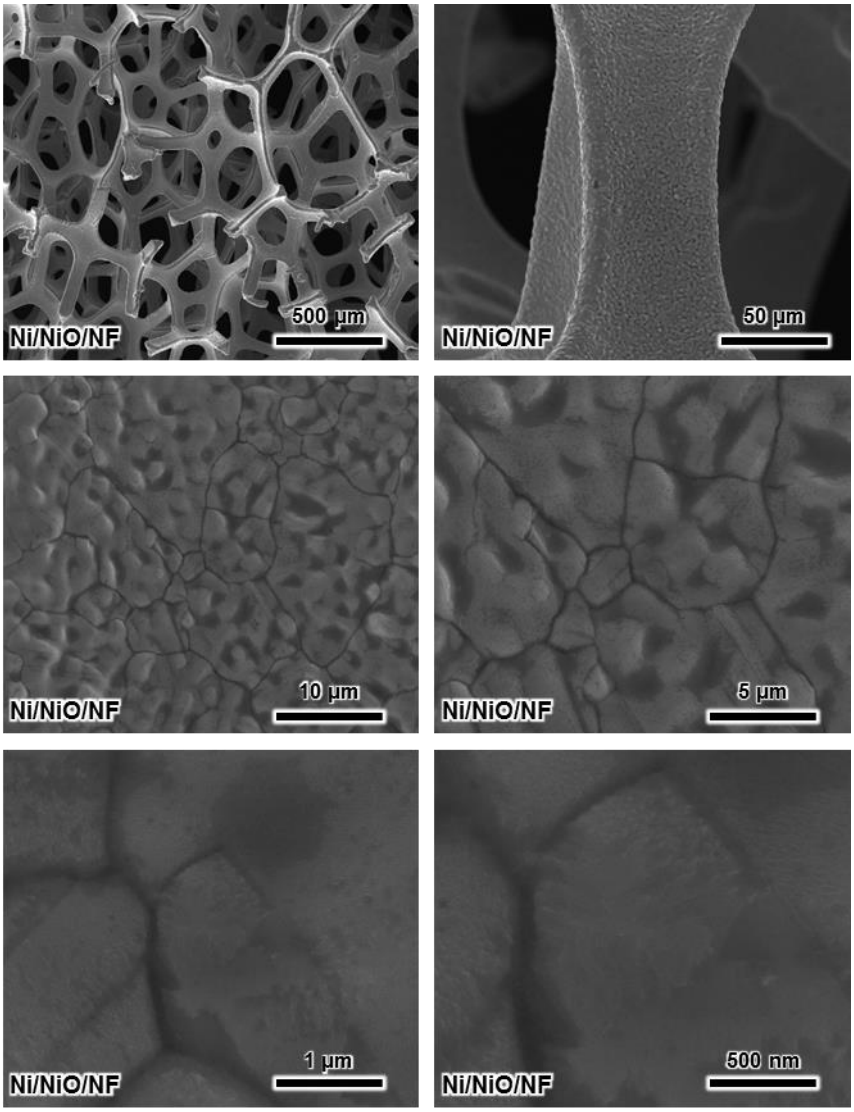

Figure S21. Full SEM characterization of NiO/Ni/NF electrode (cathode) at different magnifications after electrolysis.

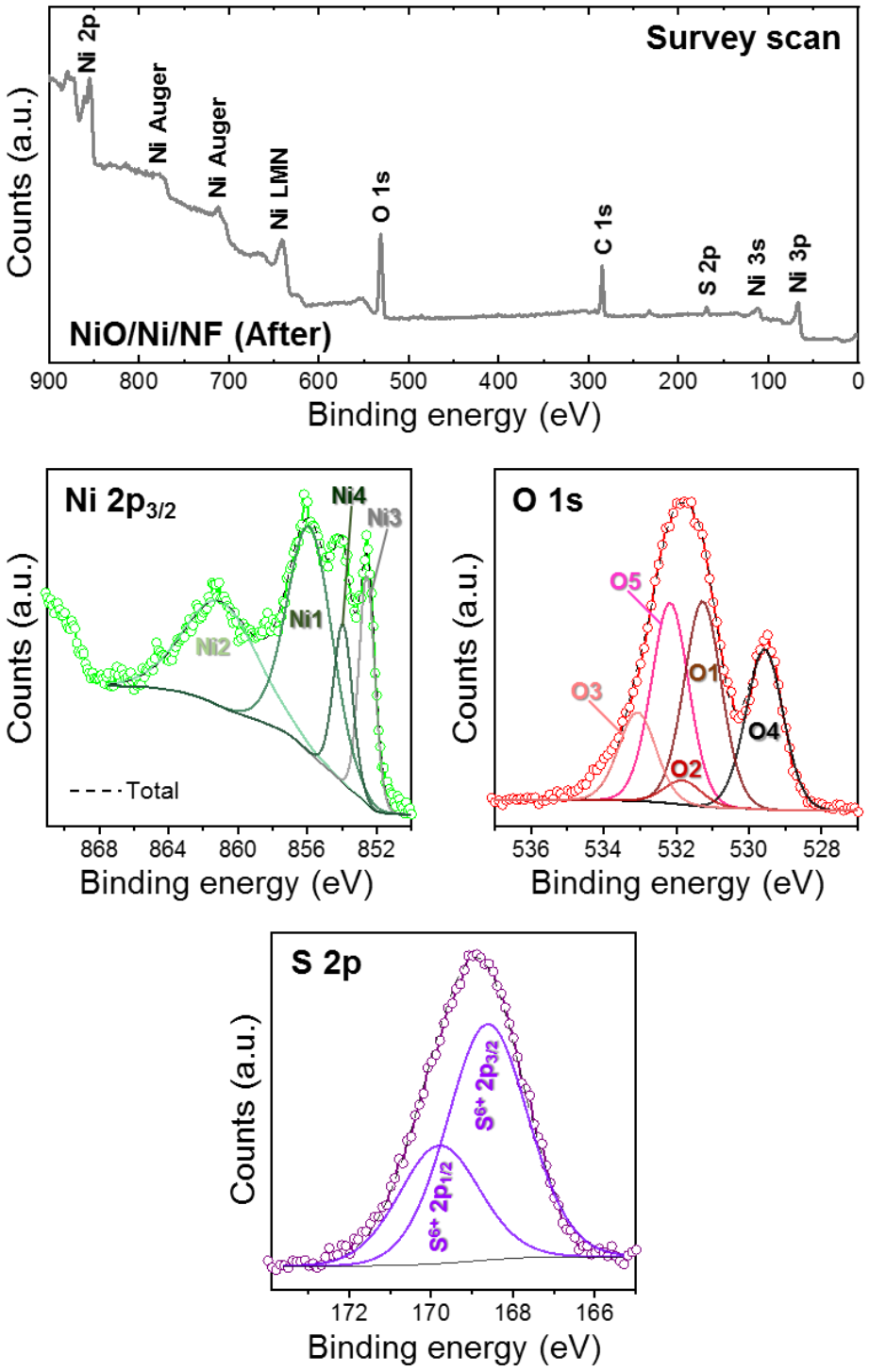

Figure S22. XPS analysis of the NiO/Ni/NF electrode after electrolysis.

Fitting the Ni $2p_{3/2}$ spectrum requires four components: (i) Ni metal [852.52 eV (Ni3)], (ii) NiO [853.89 eV (Ni4)], (iii) $Ni(OH)_2$ [855.80 eV (Ni1)], and (iv) satellites [860.94 eV (Ni2)].[16,17,25] The O 1s spectrum was deconvoluted into five components that correspond to NiO [529.56 eV (O4)], $Ni(OH)_2$ [~ 531 eV (O1)], O=C linkage [~ 532 eV (O2)], adsorbed SO_4^{2-} ions [532.16 eV (O5)], and O–C linkage [~ 533 eV (O3)].[16–18,25] The S $2p_{3/2–1/2}$ double peaks are at 168.61 and 169.79 eV, which indicates the presence of SO_4^{2-} ions due to the crossover issue.[26,27] No other signals related to metal sulfides were seen.

Surprisingly, Ni metal and NiO appeared after electrolysis. Hence, some portion of the $Ni(OH)_2$ on the NF surface might be transformed into Ni metal due to the reducing environment:

$$Ni(OH)_2 + e^- \rightarrow NiO + H_2O \quad (1)$$

$$NiO + 2e^- \rightarrow Ni + O^{2-} \quad (2)$$

According to the report about the P-substituted $CoSe_2$ pre-catalyst,[28] the structural transformation from P-substituted $CoSe_2$ into metallic Co (real reactive species) during HER testing was observed. In our case, the formed Ni metal may act as the HER active sites, which might contribute to the superior HER activity. In other words, it can be inferred that the initial $Ni(OH)_2$ is a HER pre-catalyst and the Ni metal formed after electrolysis forms the “real active sites” for the HER.

References

(1) Márquez-Montes, R. A.; Collins-Martínez, V. H.; Pérez-Reyes, I.; Chávez-Flores, D.; Graeve, O. A.; Ramos-Sánchez, V. H. Electrochemical Engineering Assessment of a Novel 3D-Printed Filter-Press Electrochemical Reactor for Multipurpose Laboratory Applications. *ACS Sustain. Chem. Eng.* **2020**, *8* (9), 3896–3905. https://doi.org/10.1021/acssuschemeng.9b07368.

(2) Márquez-Montes, R. A.; Orozco-Mena, R. E.; Lardizábal-Gutiérrez, D.; Chávez-Flores, D.; López-Ortíz, A.; Ramos-Sánchez, V. H. Sulfur Dioxide Exploitation by Electrochemical Oxidation of Sulfite in Near-Neutral PH Electrolytes: A Kinetics and Mechanistic Study. *Electrochem. Commun.* **2019**, *104*, 106481. https://doi.org/10.1016/j.elecom.2019.106481.

(3) Márquez-Montes, R. A.; Orozco-Mena, R. E.; Camacho-Dávila, A. A.; Pérez-Vega, S.; Collins-Martínez, V. H.; Ramos-Sánchez, V. H. Optimization of the Electrooxidation of Aqueous Ammonium Sulfite for Hydrogen Production at Near-Neutral PH Using Response Surface Methodology. *Int. J. Hydrogen Energy* **2020**, *45* (27), 13821–13831. https://doi.org/10.1016/j.ijhydene.2019.08.213.

(4) Levenspiel, O. *Chemical Reaction Engineering*, Third.; Wiley: New York, 1999.

(5) Scott, K.; Goodridge, F. *Electrochemical Process Engineering A Guide to the Design of Electrolytic Plant*; Springer Science+ Business Media: New York, 1995.

(6) Joshi, A. S.; Dincer, I.; Reddy, B. V. Effects of Various Parameters on Energy and Exergy Efficiencies of a Solar Thermal Hydrogen Production System. *Int. J. Hydrogen Energy* **2016**, *41* (19), 7997–8007. http://dx.doi.org/10.1016/j.ijhydene.2016.01.025.

(7) Zhang, Q.; Wang, S.; Zhu, P.; Wang, Z.; Zhang, G. Full-Scale Simulation of Flow Field in Ammonia-Based Wet Flue Gas Desulfurization Double Tower. *J. Energy Inst.* **2018**, *91* (4), 619–629. https://doi.org/10.1016/j.joei.2017.02.010.

(8) Gao, X.; Ding, H.; Du, Z.; Wu, Z.; Fang, M.; Luo, Z.; Cen, K. Gas–Liquid Absorption Reaction between (NH4)2SO3 Solution and SO2 for Ammonia-Based Wet Flue Gas Desulfurization. *Appl. Energy* **2010**, *87* (8), 2647–2651. https://doi.org/10.1016/j.apenergy.2010.03.023.

(9) Jia, Y.; Zhong, Q.; Fan, X.; Wang, X. Kinetics of Oxidation of Total Sulfite in the Ammonia-Based Wet Flue Gas Desulfurization Process. *Chem. Eng. J.* **2010**, *164* (1), 132–138. https://doi.org/10.1016/j.cej.2010.08.041.

(10) Yan, J.; Bao, J.; Yang, L.; Fan, F.; Shen, X. The Formation and Removal Characteristics of Aerosols in Ammonia-Based Wet Flue Gas Desulfurization. *J. Aerosol Sci.* **2011**, *42* (9), 604–614. https://doi.org/10.1016/j.jaerosci.2011.05.005.

(11) Asif, M.; Kim, W.-S. Modeling and Simulation of the Combined Removal of SO2 and CO2 by Aqueous Ammonia. *Greenh. Gases* **2014**, *4* (4), 509–527. https://doi.org/10.1002/ghg.1420.

(12) Jia, Y.; Yin, L.; Xu, Y.; Ding, X.; Sheng, G. A Model for Performance of Sulfite Oxidation of Ammonia-Based Flue Gas Desulfurization System. *Atmos. Pollut. Res.* **2015**, *6* (6), 997–1003. https://doi.org/10.1016/j.apr.2015.05.005.

(13) Jia, Y.; Yin, L.; Xu, Y.; Chen, Y.; Ding, X. Simulation of the Absorption of SO2 by Ammonia in a Spray Scrubber. *Chem. Eng. Process.* **2017**, *116*, 60–67. https://doi.org/10.1016/j.cep.2017.03.001.

(14) Huang, C.; Linkous, C. A.; Adebiyi, O.; T-Raissi, A. Hydrogen Production via Photolytic Oxidation of Aqueous Sodium Sulfite Solutions. *Environ. Sci. Technol.* **2010**, *44* (13), 5283–5288. https://doi.org/10.1021/es903766w.

(15) Guo, J.; Sun, J.; Sun, Y.; Liu, Q.; Zhang, X. Electrodepositing Pd on NiFe Layered Double Hydroxide for Improved Water Electrolysis. *Mater. Chem. Front.* **2019**, *3* (5), 842–850. https://doi.org/10.1039/C9QM00052F.

(16) He, B.; Kuang, Y.; Hou, Z.; Zhou, M.; Chen, X. Enhanced Electrocatalytic Hydrogen Evolution Activity of Nickel Foam by Low-Temperature-Oxidation. *J. Mater. Res.* **2017**, *33* (2), 213–224. https://doi.org/10.1557/jmr.2017.446.

(17) Li, C.; Hou, J.; Wu, Z.; Guo, K.; Wang, D.; Zhai, T.; Li, H. Acid Promoted Ni/NiO Monolithic Electrode for Overall Water Splitting in Alkaline Medium. *Sci. China Mater.* **2017**, *60* (10), 918–928. https://doi.org/10.1007/s40843-017-9089-y.

(18) Liu, C.-H.; Tang, Y.-J.; Wang, X.-L.; Huang, W.; Li, S.-L.; Dong, L.-Z.; Lan, Y.-Q. Highly Active Co–Mo–C/NRGO Composite as an Efficient Oxygen Electrode for Water–Oxygen Redox Cycle. *J. Mater. Chem. A* **2016**, *4* (46), 18100–18106. https://doi.org/10.1039/C6TA07952K.

(19) Liu, S.; Xiao, W.; Wang, J.; Zhu, J.; Wu, Z.; Xin, H.; Wang, D. Ultralow Content of Pt on Pd–Co–Cu/C Ternary Nanoparticles with Excellent Electrocatalytic Activity and Durability for the Oxygen Reduction Reaction. *Nano Energy* **2016**, *27*, 475–481. https://doi.org/10.1016/j.nanoen.2016.07.038.

(20) Xiao, W.; Cordeiro, M. A. L.; Gong, M.; Han, L.; Wang, J.; Bian, C.; Zhu, J.; Xin, H. L.; Wang, D. Optimizing the ORR Activity of Pd Based Nanocatalysts by Tuning Their Strain and Particle Size. *J. Mater. Chem. A* **2017**, *5* (20), 9867–9872. https://doi.org/10.1039/C7TA02479G.

(21) Wang, N.; Tao, B.; Miao, F.; Zang, Y. Electrodeposited Pd/Graphene/ZnO/Nickel Foam Electrode for the Hydrogen Evolution Reaction. *RSC Adv.* **2019**, *9* (58), 33814–33822. https://doi.org/10.1039/C9RA05335B.

(22) Liang, Z. X.; Zhao, T. S.; Xu, J. B.; Zhu, L. D. Mechanism Study of the Ethanol Oxidation Reaction on Palladium in Alkaline Media. *Electrochim. Acta* **2009**, *54* (8), 2203–2208. https://doi.org/10.1016/j.electacta.2008.10.034.

(23) Colón-Mercado, H. R.; Hobbs, D. T. Catalyst Evaluation for a Sulfur Dioxide-Depolarized Electrolyzer. *Electrochem. Commun.* **2007**, *9* (11), 2649–2653. https://doi.org/10.1016/j.elecom.2007.08.015.

(24) Shalom, M.; Ressnig, D.; Yang, X.; Clavel, G.; Fellinger, T. P.; Antonietti, M. Nickel Nitride as an Efficient Electrocatalyst for Water Splitting. *J. Mater. Chem. A* **2015**, *3* (15), 8171–8177. https://doi.org/10.1039/C5TA00078E.

(25) Teng, X.; Wang, J.; Ji, L.; Tang, W.; Chen, Z. Hierarchically Structured Ni Nanotube Array-Based Integrated Electrodes for Water Splitting. *ACS Sustain. Chem. Eng.* **2018**, *6* (2), 2069–2077. https://doi.org/10.1021/acssuschemeng.7b03499.

(26) Ou, X.; Luo, Z. One-Step Synthesis of Ni3S2 Nanoplatelets on Graphene for High Performance Supercapacitors. *RSC Adv.* **2016**, *6* (13), 10280–10284. https://doi.org/10.1039/C5RA22426H.

(27) Ganesan, P.; Sivanantham, A.; Shanmugam, S. Inexpensive Electrochemical Synthesis of Nickel Iron Sulphides on Nickel Foam: Super Active and Ultra-Durable Electrocatalysts for Alkaline Electrolyte Membrane Water Electrolysis. *J. Mater. Chem. A* **2016**, *4* (42), 16394–16402. https://doi.org/10.1039/C6TA04499A.

(28) Zhu, Y.; Chen, H.-C.; Hsu, C.-S.; Lin, T.-S.; Chang, C.-J.; Chang, S.-C.; Tsai, L.-D.; Chen, H. M. Operando Unraveling of the Structural and Chemical Stability of P-Substituted CoSe2 Electrocatalysts toward Hydrogen and Oxygen Evolution Reactions in Alkaline Electrolyte. *ACS Energy Lett.* **2019**, *4* (4), 987–994. https://doi.org/10.1021/acsenergylett.9b00382.